Electronic Transport of Recrystallized Freestanding Graphene Nanoribbons

Zhengqing John Qi,[†] Colin Daniels,[‡] Sung Ju Hong,[†,§] Yung Woo Park,[*,§] Vincent Meunier,[‡] Marija Drndić,[*,†] and A. T. Charlie Johnson[*,†]

[†]Department of Physics and Astronomy, University of Pennsylvania, Philadelphia, Pennsylvania 19104, United States, [‡]Department of Physics, Applied Physics, and Astronomy, Rensselaer Polytechnic Institute, Troy, New York 12180, United States, and [§]Department of Physics and Astronomy, Seoul National University, 1 Gwanak-ro, Gwanak-gu, Seoul, 151-747, Korea

ABSTRACT The use of graphene and other two-dimensional materials in next-generation electronics is hampered by the significant damage caused by conventional lithographic processing techniques employed in device fabrication. To reduce the density of defects and increase mobility, Joule heating is often used since it facilitates lattice reconstruction and promotes self-repair. Despite its importance, an atomistic understanding of the structural and electronic enhancements in graphene devices enabled by current annealing is still lacking. To provide a deeper understanding of these mechanisms, atomic recrystallization and electronic transport in graphene nanoribbon (GNR) devices are investigated using a combination of experimental and theoretical methods. GNR devices with widths below 10 nm are defined and electrically measured *in situ* within the sample chamber of an aberration-corrected transmission electron microscope. Immediately after patterning, we observe few-layer polycrystalline GNRs with irregular sp^2-bonded edges. Continued structural recrystallization toward a sharp, faceted edge is promoted by increasing application of Joule heat. Monte Carlo-based annealing simulations reveal that this is a result of concentrated local currents at lattice defects, which in turn promotes restructuring of unfavorable edge structures toward an atomically sharp state. We establish that intrinsic conductance doubles to 2.7 e^2/h during the recrystallization process following an almost 3-fold reduction in device width, which is attributed to improved device crystallinity. In addition to the observation of consistent edge bonding in patterned GNRs, we further motivate the use of bonded bilayer GNRs for future nanoelectronic components by demonstrating how electronic structure can be tailored by an appropriate modification of the relative twist angle of the bonded bilayer.
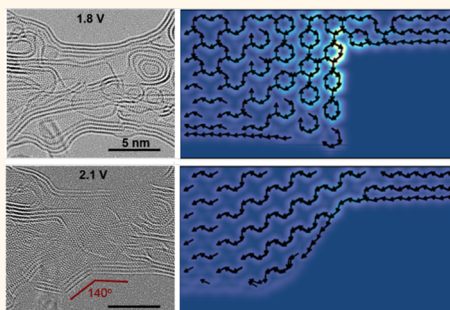
KEYWORDS: graphene nanoribbons · *in situ* transmission electron microscopy · nanosculpting · reconstruction · accelerated annealing simulation

For decades, the semiconductor industry has been following Moore's law as the golden standard for chip design and manufacturing.[1] The miniaturization of device components based on copper and silicon has become one of the key driving principles in enabling smaller devices with greater performance, improved power consumption, and reduced production costs.[2] However, the scaling of both silicon and copper nanostructures is approaching its intrinsic limits, and the introduction of new materials is needed to ensure continued gains in performance.[3] Among the potential candidates, graphene-based structures have emerged as novel materials that could replace silicon and/or copper due to their unique electronic properties.[4−9] Unlike two-dimensional graphene, graphene nanoribbons (GNRs) can present an electronic band gap and are therefore particularly promising for future integrated circuit (IC) device components such as on-chip electrical interconnects,[10,11] transistor channels,[12,13] and sensors.[14−16] The GNR's edge structure dictates the electrical characteristics in these applications,[17] and it is the goal of the present work to provide a fundamental understanding of the atomistic mechanisms governing the edge structure reconstruction and its dynamics.

Bottom-up approaches offer the possibility to devise essentially defect-free GNR systems, but efforts to systematically measure their intrinsic two-terminal transport properties have been hindered by poorly developed techniques to transfer GNRs from the catalytic metallic growth substrate onto adequate dielectric materials.[18,19] Alternatively, a number of top-down

* Address correspondence to
ywpark@phya.snu.ac.kr,
drndic@physics.upenn.edu,
cjohnson@physics.upenn.edu.

approaches have been proposed to pattern graphene to IC-relevant length scales below 10 nm, including electron beam lithography,[20] nanowire[21] and gold etch masks,[22] scanning tunneling microscope lithography,[23] and block copolymer lithography.[24] However, the absence of a top-down patterning solution that allows for precise control of atomic edge terminations has resulted in device-to-device variability due to the sensitivity of electronic structure on edge geometry.[25−27]

In this context, recent efforts using a focused electron beam have enabled a pathway for atomic scale patterning. Efficient subnanometer resolution "nanosculpting" of suspended graphene sheets within a transmission electron microscope (TEM) has been demonstrated using a focused electron beam[28−31] with energies above graphene's knock-on damage threshold (∼86 keV).[32] This has enabled the controlled patterning of suspended monolayer graphene nanostructures[33] and has provided a unique platform[34] for in situ transport measurements of sub-10 nm monocrystalline GNR devices fabricated within the TEM.[35] Notably, previous work utilizing thermal annealing to motivate structural recrystallization[36,37] and self-repair[30,38,39] in suspended graphene sheets was leveraged for the successful fabrication of crystalline GNR devices via current-induced Joule heating.[34,35,40−42]

Despite the critical importance of annealing in forming defect-free GNRs, the recrystallization mechanism and its direct impact on intrinsic device transport properties remain to be clearly explained and quantified. Progress has been made difficult due to the lack of experimental approaches to simultaneously probe the atomic structure of the actual device as it is electrically characterized. This highlights the new opportunity explored in this work where we provide a fundamental and quantitative understanding of current-induced recrystallization and its influence on atomic structure and electrical transport in isolated sub-10 nm GNR devices. In addition, results from this work yield relevant and practical design recommendations applicable to a broad range of GNR-based applications.

In this article, we combine simultaneous real-time TEM nanostructuring with two-terminal electronic transport measurements on GNRs to understand the reconstruction mechanism of single-nanometer-scale GNR devices probed in situ. We observe that, immediately after patterning, sub-10 nm few-layer ribbons are polycrystalline, with rough, sp²-bonded bilayer edges, providing a suitable isolated system for monitoring the physical and electrical progression toward recrystallization. Bias-controlled Joule-heating encourages the GNR's structural evolution toward faceted, bonded bilayer edges and the eventual assimilation of structural protrusions into the bulk, presenting a crystalline junction-free GNR. The observations are consistent with simulations showing that amorphous regions

and lattice defect sites experience the greatest heat dissipation during current annealing and are therefore most susceptible to recrystallization. The GNR conductance is found to double to 2.7 e^2/h during the GNR recrystallization process, where e is the electron charge and h is Planck's constant, despite an almost 3-fold reduction in the device width to ∼3 nm. The enhanced conductance is attributed to improved structural order in the recrystallized GNR, compensating for the narrower width. Despite achieving superior transport and crystallinity, GNR edges remain bonded throughout recrystallization, thereby preventing the engineering of electronic structure through edge doping or modification of the edge-termination geometry. In addition to edge structure, the relative orientation of stacked graphene monolayers plays a critical role in determining the electronic properties of the bilayer.[43] TEM imaging is used to determine the relative orientation of individual graphene layers within bilayer stacks, and we use this information as an input for simulations of how electronic structure can be tailored by manipulating the relative angle between two adjacent monolayers (i.e., the twist angle) in bonded bilayer GNRs. Here the twist angle is locked by the details of the covalent bonding between the adjacent layers. Experimentally, a variety of twist angles are observed after current annealing, indicating the feasibility of fabricating bonded bilayers with unique orientations. Tight-binding calculations confirm that bonded bilayer GNRs of different twist angles offer a diverse set of electronic properties, ranging from purely metallic systems to semiconductors with a sizable band gap (0.25 eV).

RESULTS AND DISCUSSION

Experiments are based upon CVD-grown graphene,[44,45] patterned into a freestanding ribbon contacted by source-drain Au electrodes[46] (Figure 1a). Figure 1b shows a TEM micrograph of a freestanding graphene ribbon, ∼700 nm wide, within the experimental setup. The GNR is supported by a 100 nm thick SiN$_x$ membrane with a predefined 1 μm wide slit where the suspended GNR is formed (details are provided in the Methods section and in particular Supporting Information Figure S1). The chip is mounted on a TEM holder with electrical feed-throughs to facilitate in situ electrical transport measurements within an aberration corrected TEM. TEM imaging and electrical measurements are performed in high vacuum (10^{-7} Torr) at room temperature using a FEI-Titan 80−300 TEM with an objective lens CEOS aberration corrector, operated at 300 kV. Measured values of device resistance for as-fabricated devices are found to be ∼70 kΩ. Current annealing is performed within the TEM before further sample characterization; this is done to remove unwanted residue and contaminants from sample fabrication[47] and to minimize electron beam-induced deposition of amorphous carbon.[48] A slow voltage

ramp of 5 mV/s is used to increase the current to ∼100 μA, resulting in high-temperature resistive heating in the graphene ribbon. Vaporization of surface contaminants and edge reconstruction is observed (Supporting Information Figure S2), consistent with previous observations in thermally annealed graphene sheets,[36,37] resulting in a final device resistance of <10 kΩ (Figure 1c).

A patterning technique using a condensed electron beam is subsequently used to reduce the width of the annealed devices within the TEM.[35] Specifically, a 300 kV electron beam (focused to minimum diameter <5 nm) is used to progressively sculpt the suspended

graphene down to a 10 nm width through direct knock-on damage (Figure 1d). A bias voltage between 1 and 3 V is applied across the GNR during this sculpting procedure, to prevent electron beam induced hydrocarbon contamination.[30] The nanosculpting and measurement procedures are used for *in situ* production of few-layered GNRs with critical dimensions between 10 to 500 nm. We highlight typical results of nanosculpting in Figure 1d, with ablated areas highlighted in red. We apply this patterning technique repeatedly on individual GNRs and measure the *in situ* two-terminal resistance as a function of width (Figure 1c inset). We fit the resistance data with an equation of the form $R_{TOT} = R_C + \rho/w$. R_C is the contact resistance that accounts for the resistance of the wiring, gold–graphene interface, and wide graphene regions outside the GNR; w is the width of the GNR, and ρ is a fitting parameter with the units of resistivity. This form, appropriate for an Ohmic conductor, provides a good fit to the data as the width is reduced from 500 to 10 nm (Figure 1c inset), with an extracted contact resistance of R_C = 10.9 kΩ. After the GNRs are narrowed to ∼10 nm, their resistance is further recorded while the conductor is simultaneously imaged until the moment it breaks and the resistance increases beyond the limit of the measurement system.

High edge contrast is consistently observed in patterned GNRs, as expected for increased electron scattering from a continuous, curved, sp²-bonded bilayer edge.[49,50] This hypothesis is experimentally supported by the images in Figure 2, which are derived from as-transferred graphene material that was not subject to nanosculpting. Figure 2a shows a graphene bilayer, where the (free, low-contrast) edges of the graphene layers are separated by ∼5 nm. Two-dimensional fast Fourier transforms (2D FFTs; Figure 2b and Supporting Information Figure S4) are used to identify the number of carbon layers in each region, and they show a transition from bilayer graphene to monolayer
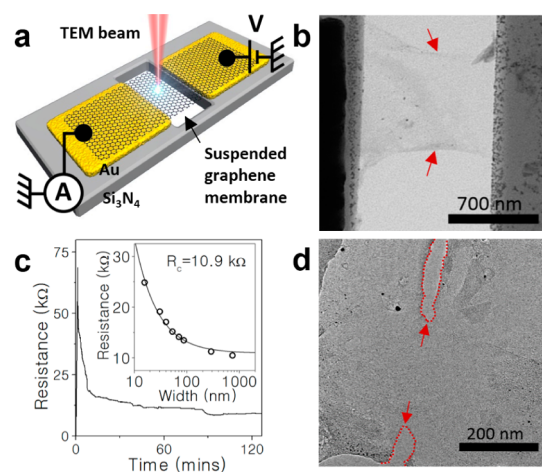

Figure 1. Device layout, current annealing, and nanosculpting. (a) Schematic of TEM-compatible chip with a suspended graphene device contacted by source and drain electrodes. **(b)** TEM micrograph of patterned suspended graphene ribbon. Arrows indicate the edges of the ribbon. **(c)** Time evolution of device resistance during current annealing. Inset: Two-terminal GNR resistance as a function of width (*w*) for *w* > 10 nm with solid curve showing the fit to the form $R_{TOT} = R_C + \rho/w$ (see main text). **(d)** TEM micrograph of graphene after nanosculpting. The sculpted region is highlighted in red, and red arrows indicate the edges of the narrowed graphene region.
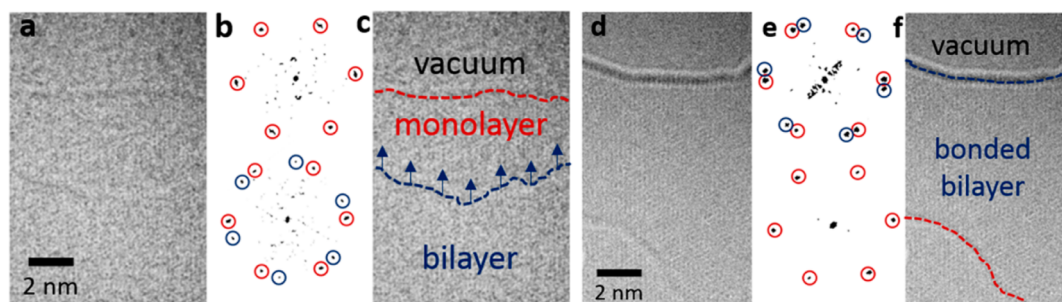

Figure 2. TEM images and 2D FFTs of a monolayer graphene platelet before and after bonding to its monolayer substrate. (a) TEM image of a monolayer graphene platelet supported by a monolayer graphene substrate. **(b)** 2D FFT from panel (a), taken from regions of the graphene substrate (top) and bilayer area (bottom) showing one and two distinct 6-fold FFT peaks, respectively, highlighted in red (substrate) and blue (platelet). **(c)** Dotted lines drawn over the TEM image in (a) to indicate the boundary between vacuum and the graphene substrate (red) and between the graphene substrate and bilayer region (blue). Arrows indicate the direction the platelet moves to bond with the monolayer edge. **(d)** TEM image after edge bonding. **(e)** Corresponding 2D FFT of (d) taken from regions of the bonded bilayer substrate (top) and monolayer substrate (bottom) showing two and one distinct 6-fold FFT peaks, respectively, and highlighted in red (substrate) and blue (platelet). **(f)** Dotted lines drawn over the TEM image in (d) to indicate the boundary between vacuum and the bonded bilayer graphene (blue) and between the bilayer region and monolayer graphene substrate (blue).
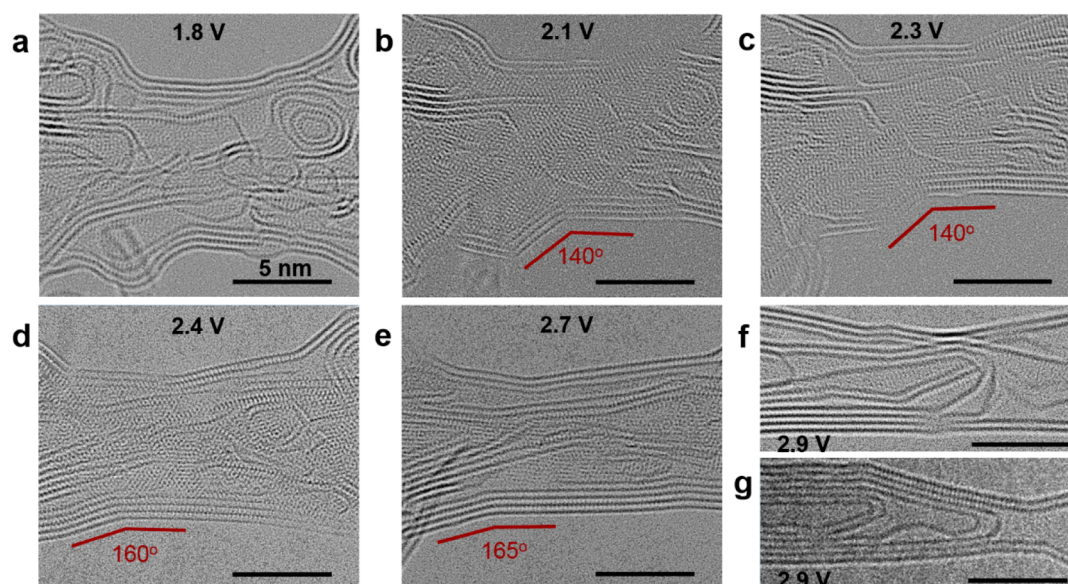
Figure 3. Current induced recrystallization in few-layer (≥4 layers) GNR devices. (a) TEM micrographs of an isolated few-layer GNR (w = 8.2 nm) under bias. Initial structure showed rounded semi-amorphous edges. (b) Evolution of (a) showing the width narrowing to 7.7 nm, structural recrystallization, and the formation of atomically sharp edges after high-bias Joule heating. (c−e) Evolution of (b) showing the width narrowing to 7.1 nm (c) and the continued flattening of the protruding edge (d,e). (f,g) Final evolution of the GNR showing two stacked bonded-bilayers before device breakdown (w = 3 nm). Scale bar is 5 nm in all images.

graphene to vacuum (Figure 2c). From this, we conclude that the red dotted line represents the edge of a base monolayer sheet, which supports a second carbon layer, whose (free) edge is indicated by the blue dotted line (Figure 2c). The supported graphene sheet is apparently free to travel along the base monolayer, and eventually bonds with the free edge, resulting in an increase in contrast for the top bonded bilayer edge (Figure 2d).[51] This interpretation is consistent with the 2D FFT, which shows that the high-contrast (now, bonded) edge marks the transition from vacuum to bilayer, while a low-contrast edge (red dashed line) occurs at the interface between a bilayer region and a monolayer region. This indicates that high contrast edges observed in these experiments represent bonded bilayers rather than the edges of monolayer sheets,[52] in contrast to past suggestions made using a somewhat similar experimental setup.[36,51] Using this insight, GNR edges produced by nanosculpting are consistently bonded (Figure 3a) and remain so throughout recrystallization (Figure 3b−d). Because of the reactivity of dangling bonds at the edges of pristine GNRs, it is likely that a bonded bilayer will immediately form after overlaying a second GNR, or when edges are exposed immediately after etching. This highlights a fundamental limitation for efforts to fabricate bilayer GNR devices with free edges. However, since bonded bilayer GNRs offer roughly five times greater intrinsic conductivity and superior structural stability as compared to monolayer GNRs of comparable widths,[35] this motivates the idea of circuitry based on bonded bilayer GNRs, avoiding the need to consider edge passivation.

Top-down patterning of graphene naturally induces edge disorder due to the absence of atomic-resolution etching capabilities. Previous theoretical works revealed a substantial reduction in thermal conductivity and transport properties for GNRs with relatively small values of edge roughness[53] and edge/bulk disorder,[54] motivating the need for a controllable process to fabricate highly crystalline GNRs. At the same time, we should note that devising a way to improve electronic transport while keeping thermal conductivity low would be ideal to develop GNR-based thermoelectrics. This could be done by reaching a fine balance between increase electronic mean free-path while preserving sufficient amorphous edges to scatter phonons.[55]

We find that sub-10 nm GNR devices patterned by means of a focused electron beam are inherently disordered and polycrystalline (Figure 3a) in agreement with prior report of direct knock-on induced damage.[56] We show that the transformation from a disordered rough structure (Figure 3a) to a highly crystalline GNR (Figure 3e−g), which will be referred to as structural recrystallization, can be intentionally and controllably induced. We explore the recrystallization process of few-layer GNR devices with bonded edges by systematically increasing the bias voltage (100−300 mV steps) applied to the GNRs immediately after patterning, elevating the ribbon's temperature due to resistive heating, until device breakdown. Temperatures of ~2000 K are typical during reconstruction, as evaluated in the Supporting Information and observed previously.[36,37,50] The beam energy used to observe the annealing process is high enough to lead

to knock on damage, but the beam current is too low to account for the structural changes observed during the experiment (a calculation of the sputtering rate is provided in the Supporting Information).

Figure 3 shows the time evolution of a representative multilayer GNR device as its width is reduced from 8.2 nm (Figure 3a) to 3 nm (Figure 3g) under increasing electrical stress (Joule heating), from 1.8 to 2.9 V, as well as its continued structural recrystallization. The reconstruction process takes place primarily along the GNR boundary, where the initial curved edge morphology (Figure 3a) recrystallizes to become faceted (Figure 3b). Further Joule heating leads to the flattening of the protruding edges (Figure 3c–f), as indicated by the measured junction angles noted in red. The continued sharpening in edge morphology is attributed to the larger electrical resistance in edge junctions,[36,57] allowing for greater heat dissipation and increased susceptibility to recrystallization, as revealed by the simulations discussed below. At a bias of 2.9 V, the width of the ribbon abruptly narrows down due to increased atomic dislocations induced by the intensifying electrical stress per bond. This process is accompanied by a layer-by-layer breaking of the stacks (Figure 3e–g). The device thickness can be accurately determined by distinguishing the number of edges in each GNR from the micrographs. The initial structure presents four discernible edges (Figure 3a–d), representing four stacked bonded bilayers with a total thickness of ∼1.4 nm. The device is reduced to two bilayers after continued electrical stress (Figure 3e–g) and ultimately is severed.

Motivated by the experimental observations, the physical evolution of a representative bonded bilayer GNR system is modeled using an original Monte Carlo algorithm that simulates annealing over a larger time scale compared to that of traditional molecular dynamics approaches. The algorithm, known as the accelerated topological annealing of carbon (ATAC), applies elementary defects to an input system in a stochastic manner.[58,59] ATAC accepts or rejects the defects based on the change in system energy as evaluated using a parametrized interatomic potential.[60,61] This approach leads to knowledge of the structural evolution and the possibility to monitor the variations of physical properties at the main steps of the structural transformation. In particular, the electronic properties are evaluated using a computationally inexpensive π-band tight binding method with a nearest-neighbor approximation, and $\gamma_0 = -2.7$ eV, sufficient for carbon-only, sp^2-bonded, nonmagnetic structures.[62,63] Conductance and density of states are calculated using a combination of the Landauer formalism,[64] standard Green's functions,[65] and transfer-matrix-based approaches.[66–68] Simulation parameters (i.e., temperature schedule and relative occurrence of knock-off atoms versus bond rotations)

for the structural simulation are chosen to best match the observed behavior as seen in Figure 3a,b. Note that only the effects of Joule heating to the system as a whole are considered in the simulation, and that effects such as localized heating due to electrical stress are omitted.

The ATAC algorithm uses an input nanosystem and records its structure in the form of an undirected graph using the system's adjacency matrix (i.e., its list of first-neared neighbors). ATAC then randomly applies structural mutations from a provided catalog (see below) to the structure by modifying the system's graph and enforcing the corresponding bond structure modifications via a penalty potential function. The applied mutations are then accepted or rejected based on a probability distribution, similar to Arrhenius' equation, which is a function of an artificial simulation temperature and the difference in energy introduced by the mutation as measured by a parametrized interatomic potential.[58,59] Note that after each mutation is enacted, the entire system is structurally relaxed before the difference in energy due to the mutation is calculated.

The catalog of possible structural mutations includes four different types of local transformations of the system's adjacency matrix. Each mutation is attempted with specified rates of occurrence, chosen depending on assumptions on the available energy imparted to the system and the type of experimental process (e.g., Joule heating vs electron bombardment). The most common one is the single atom vacancy, which consists of simply removing a carbon atom from the system. Here it accounts for 35% of the total attempted mutations. The second most commonly attempted mutation is the Stone−Thrower−Wales bond rotation (which transforms 4 adjacent hexagons into two pentagons separated by two abutting heptagons), comprising 25% of attempted mutations. The last two types are bond addition and bond removal, at 20% each. These mutations consist of either attempting to enforce or dissociate a bond between nearby carbon atoms. In practice, because acceptance and rejection of an attempted mutation by ATAC depends entirely on the change in system energy it introduces, the types of accepted mutations during the course of the actual simulations can vary considerably from the imposed rates of attempted mutations. In addition, it is worth mentioning that it is the complex multistep introduction of stochastic events at random positions within the structure that leads to a realistic description of the structural evolution.

Here, the input structure fed into ATAC is a zigzag oriented bonded bilayer GNR with an amorphous protrusion at 90°. This initial configuration is chosen to correspond to a system with an energetically unfavorable edge structure, similar to Figure 3a. Figure 4a–c displays representative results for the evolution of both local currents and structure as the
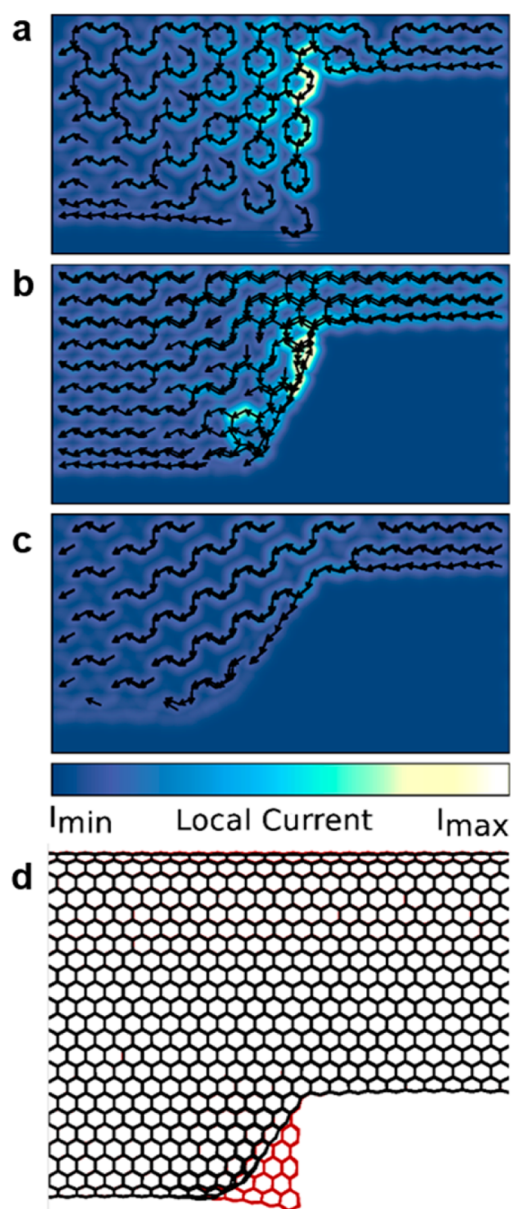
Figure 4. Simulated bonded bilayer GNR edge recrystallization and local current calculations using chemical potentials of 0.1 eV to highlight electronic properties near the Fermi energy. Arrows indicate the local current direction when its magnitude is within 90% of the maximum. The simulations were realized at constant bias potential. The color bar represents data with identical range of values. (a) Local current of initial structure showing a large current magnitude near the 90° junction. This junction features the highest local current amplitude, at the knee-like region of the joint. (b) Intermediate structure showing reduction of the highly localized current. (c) Final structure showing further reduction in local current magnitude. In this case, the structure behaves like a more uniform system where electronic current flows equality over the entire structure. Note that the overall current, that is, the current integrated over any cross-section of the systems, remains almost constant between the three structures, due to the fact that the structures were overall quite crystalline to begin with. (d) Top-down structural plot showing the schematic of the initial amorphous edge (red) and after annealing (black).

bonded bilayer system was annealed *via* ATAC. The local current is computed using the well-established

theoretical framework, using a tight-binding Hamiltonian recomputed at each stage of the evolution.[69] As the system anneals, the bonded bilayer GNRs are seen to progress consistently toward a state with atomically sharp edges. This reconstruction is fueled by the preference for irradiation-induced defects (vacancies in particular) to nucleate close to the rough edges since they tend to stabilize the structure. The local current density plot of the initial structure shows a large magnitude near the 90° bonded bilayer edge, which corresponds to the greatest heat dissipation and, in turn, greatest susceptibility to recrystallization (Figure 4a). As the system anneals, the bonded bilayer GNR evolves toward a state with atomically sharp edges due to the defective lattice sites at the GNR edge being the most susceptible to ejection and additional defects.

The continued edge recrystallization leads to increased structural stability. In addition. we note that while the maximum local current density decreases during structural evolution, the largest value of the current remains maximal close to the transitional region between straight segments. This indicates that the structure should tend toward presenting a single continuous edge over longer evolution periods as seen in Figure 3g and Figure S2 in the Supporting Information. In light of the local current and structural annealing results, it is expected that accounting for localized heating effects, as were present in the experiment itself, would only increase the instability of defective sites at the bonded bilayer GNR edge. This marked tendency toward edge defects, and the energetic favorability of the crystallized edge structure, accounts for many of the experimentally observed behaviors, and those shown in Figure 3a−c in particular.

Intrinsic electrical properties of the GNR shown in Figure 3 are extracted during the recrystallization and breakdown processes (Figure 5). We highlight the breakdown regime in tan color in Figure 5a,b. During recrystallization, the intrinsic conductance (resistance) progressively increases (decreases), suggesting the initially disordered GNR becomes increasingly more crystalline, with reduced carrier scattering and improved transport that compensates for the reduction in device width. During the breakdown phase, the crystalline GNR narrows further and eventually breaks due to extreme electrical stress, but does not further recrystallize, since it is already highly ordered at that stage.

Turning back to experiment, the initial resistance of the GNR, after nanosculpting and before annealing is 19 kΩ (Figure 5a). This resistance decreases in steps during the recrystallization process to a minimum of 8 kΩ, as the GNR width reduced from 8.2 to 5.4 nm. For widths below 5 nm, characteristics of device breakdown are observed, and the resistance sharply increases until complete device failure. We note that
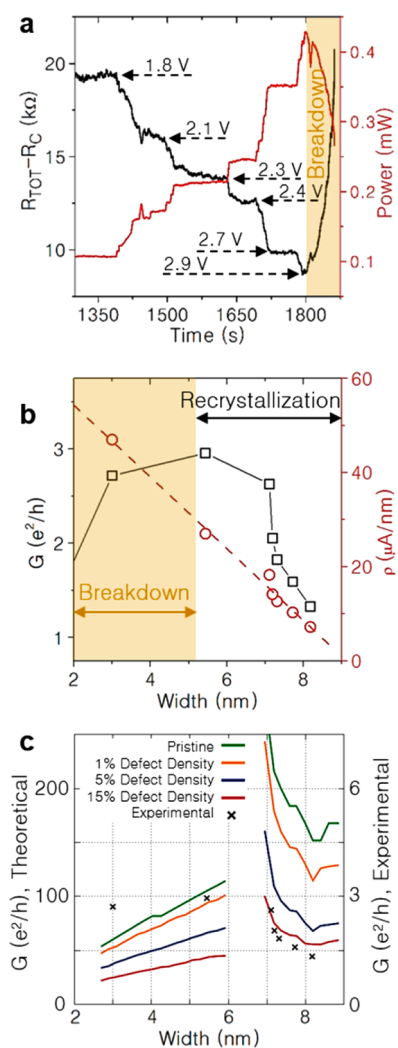
Figure 5. GNR transport during reconstruction. (a) Time evolution of two-terminal device resistance (contact resistance subtracted) and power for $w < 10$ nm with progressively higher Joule heat, as indicated by the supplied bias, until device breakdown. **(b)** Measured intrinsic conductance (black squares) and current density (red circles) as a function of width for few-layer GNRs under increasing Joule heat. Conductance values have the best-fit contact resistance subtracted. **(c)** Comparison of the measured device conductance and theoretical values obtained by a first-neighbor tight-binding method for stacked bonded bilayer GNRs of varying defect density.

multilayer GNR devices are remarkably robust, showing a resistance plateau each time the target bias has been reached (Figure 5a) and only deviates from a resistance plateau at constant bias during device breakdown. This provides the opportunity to tailor the GNR during recrystallization, by terminating the process ($V_{bias} = 0$ V) when preselected structural and electrical properties are achieved. The sample, with known atomic structure, could then be transferred from the TEM to an alternative measurement platform for more in-depth analysis, Greater sensitivity in the regulation of the source-drain bias during recrystallization can provide a more controlled recrystallization process, and could be the focus of future studies.

The power dissipated in the GNR during this process, defined as $P = I^2 (R - R_C)$, peaks at a value of 420 μW before breakdown (Figure 5a), representing a temperature in excess of 2000 K (calculations shown in the Supporting Information), similar to past reports.[37,41,50] The sustained electrical current density (μA/nm), increases even during the structural breakdown regime (Figure 5b). This is attributed to the contribution of additional conduction channels in the multilayer stack, providing an overall increase in current. This result should be contrasted with Ohmic behavior, which would result in a current decrease upon cross-section reduction, and further highlights the coherent (i.e., increased mean free path) transport regime characteristic of highly crystalline, confined nanostructures. At the GNR's narrowest width of 3 nm, a maximum current density in excess of 4.7×10^9 A/cm^2 is recorded, to our knowledge the highest current density reported so far for a four-layer GNR. Furthermore, the intrinsic conductance doubles to 2.7e^2/h during the recrystallization process despite an almost three times reduction in device width (Figure 5b). The enhanced conductance is attributed to improved carrier transport from the lower number of scattering centers present in the recrystallized GNRs, as discussed in detail below.

Simulated conductance values are obtained using the π-band tight-binding method as a comparative basis for the measured conductance. Figure 5c shows theoretical conductance values of a modeled GNR, with varying defect density, width, and thickness, along with the measured values. Defect density is defined as the number of Stone–Thrower–Wales defects introduced divided by the number of atoms in the system, and represents the level of disorder in the simulated GNR. Transport in GNRs with defect densities between 0 and 15% were used to simulate the influence of recrystallization on conductance. Structurally, a four-stack bonded-bilayer GNR was modeled for devices of widths >7 nm and two stacks were used for widths <6 nm, in correspondence to the micrographs presented in Figure 3. For particular GNR widths, the experimental voltage biases are known and utilized in the simulation, while intermediate voltage values are estimated from a linear interpolation, providing a continuous conductance vs width graph. GNRs of widths 7–9 nm show a continued increase in conductance for various defect densities, consistent with the increase of bias voltage used in the experiments to drive recrystallization. When the simulated 8-layer GNR is reduced to only 4 layers, the bias is at 2.9 V and the ribbon is allowed to spontaneously break under electrical stress, as simulated in the 3–6 nm regime.

It must be noted that the theoretical conductance consistently improves as defect density is reduced, regardless of device width or sample bias. This is expected since devices with greater structural crystallinity have superior carrier transport. Experimental

intrinsic conductance values are plotted on a 3:100 scale along with the theoretical conductance. The experimental results during recrystallization are in good agreement with the red curve corresponding to 15% defect density, while experimental results during the breakdown regime match closer with the pristine GNR (green) curve, showing the best transport properties. Although the simulated and experimental GNR systems are not identical, an overall trend can be extracted from Figure 5c. Given a system that has constant crystallinity, one would expect the experimental data to follow a single, scaled, theoretical curve. Rather, the experimental data fall nicely onto two distinctly different curves, one indicating a pristine GNR and another indicating a GNR with the highest simulated lattice disorder. That is, the increase in conductance cannot be exclusively attributed to an increasing bias, but also the improved transport due to greater structural crystallinity. The data suggest that structural crystallinity has a *major role* in improving the electrical performance of GNRs, and our recrystallization process provides a pathway for the fabrication of atomically sharp GNRs with superior transport properties.

So far, we have been able to establish that the dynamical annealing process leads to enhanced electronic transport properties. However, while superior conductance is a necessary condition for the development of nanoelectronics, it is certainly not a sufficient one. Indeed, in order to fully harness the potential of GNR devices, the electronic properties should be easily tunable and tailored to specific applications. To address this issue, we now focus on how the twist angle between adjacent layers can be used as a quasi-continuous knob to vary transmission properties, following an early theoretical proposal.[70] We observe various twist angles during the course of our experimental investigations. Figure 2 shows supported monolayer with a twist of 31° rotated clockwise to bond with its monolayer support, resulting in the final bilayer twist angle of 10° (Figure 2e). We extract an initial twist angle for the unbound bilayer to be $16 \pm 1°$ (Figure 2b). For this particular case, the supported monolayer twists by $31 \pm 1°$ clockwise in order to bond with the stationary base monolayer, resulting in the final bilayer twist angle of $10 \pm 1°$, as extracted from the 2D FFT in Figure 2e. We also find that a twist angle of 10° is certainly not universal. Varying twist angles are observed in different bonded bilayer GNRs (*e.g.*, $15 \pm 1°$, $33 \pm 1°$, and $30 \pm 1°$), as extracted from the 2D FFT in TEM micrographs presented in Supporting Information Figure S3.

Simulations are utilized to investigate how the electronic properties change as a function of the twist angles observed experimentally. Atomic structures are first obtained by connecting the edges of two GNR sections offset by 10.89°, 16.10°, 30.00°, and 33.04°, *i.e.*,

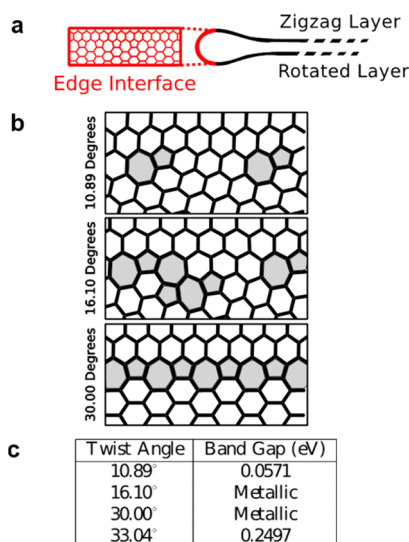| Twist Angle	Band Gap (eV)
10.89°	0.0571
16.10°	Metallic
30.00°	Metallic
33.04°	0.2497

Figure 6. Structural and electronic properties of simulated 3.5 nm bonded bilayer GNRs with varying twist angles corresponding to angles observed experimentally in Figure 2 and Figure S3. Data were obtained for twist angles of 10°, 15°, 30°, and 33°, where the bottom layer was a fixed zigzag layer, and the top was rotated by the specified angle. (a) Lateral and side views of the interface between the top and bottom layers. The red sector corresponds to the panels shown in (b). (b) Three different twist angle structures. The twist angles correspond to the introduction of a number of dislocations related to the presence of pentagon/heptagon pairs between the otherwise hexagonal lattice. The 33° system has a significantly larger unit cell size and is not shown here. (c) Table of band gap values, showing that while there is no discernible pattern within the twist angles tested, large variability can be seen.

at angles corresponding to the experimental data. The GNR structures are then annealed using ATAC to obtain a low-energy interface between the two layers. All GNRs are modeled with a width of ~3.5 nm. Figure 6b presents a side view of three unique bonded bilayer interfaces to highlight their structure and the presence of 5 and 7-atom rings running parallel to the interface (darkened for visibility). Because of its long unit cell size, the 33° twist angle structure is omitted from the figure due to size constraints. Tight-binding electronic characteristics are shown in Figure 6c. There is a clear variety in electronic structure, with a small energy gap in the GNR with an 11° twist, to pure metallic devices in GNRs with a 16° or 30° twists, to a GNR with a sizable band gap (0.25 eV) when it is twisted at 33°. The computed data also show how the twist angle allows the tailoring of band gaps in bonded-bilayer GNRs, including switching between metallic and semiconducting, and could provide a pathway for nanoelectronics solely consisting of GNRs. We should emphasize that the twist angle only indirectly governs the electronic properties. Rather, it is the detail of the covalent connection between the two twisted layers that dictates electronic behavior.

CONCLUSIONS

In summary, we demonstrated that the combination of electron beam nanosculpting and controlled Joule

heating may be used to fabricate atomically smooth freestanding graphene nanoribbon devices with superior electrical transport. By performing coordinated experiments and modeling, we developed a thorough understanding of the reconstruction mechanisms at play in single-nanometer-scale GNR devices probed *in situ*. Lattice disorder and bonded bilayer edges were observed for sub-10 nm GNR devices immediately after patterning. With increasing Joule heat, the GNR continuously recrystallized while preserving the bonded bilayer edges, and intrinsic conductance improved despite the narrowing width. The bonded bilayer edges became faceted and surface protrusions subsided into the bulk under the increasing bias. These observations were explained by simulations showing that local current maxima are concentrated at junctions, leading to a recrystallization process that encourages the structure toward sharp continuous edges. We found that intrinsic conductance *doubled* to $2.7e^2/h$ during the recrystallization process despite an almost *three times reduction* in device width, and we observed sustained current densities in excess of 4.7×10^9 A/cm^2, relevant toward future on-chip interconnects. A similar improvement in conductance was observed in simulations and attributed mainly to improved transport resulting from structural recrystallization, indicating the limitations of traditional patterning/etching procedures and the potential for Joule-heat recrystallization. In our setup, nanosculpting typically leads to GNR structures with linked edges. Similarly, other methods of patterning multilayer graphene are expected to leave the edges exposed and susceptible to bond. We provide experimental evidence of annealed bonded bilayer GNRs with varying twist angles and their associated transport properties. We also discussed how this work opens new directions for band gap engineering *via* twist-angle modification with high relevance for next-generation nanoelectronics.

METHODS

Graphene Growth. Graphene was grown *via* atmospheric pressure chemical vapor deposition on 99.999% purity copper foil in a 1 in. tube furnace.[44,45] A 100 μm thick Cu foil (Alfa Aesar, 42189) was loaded into the tube furnace (Lindberg blue M, TF55035) and heated to 1057 °C under a flow of 500 sccm of Ar (99.999%) and 50 sccm of H$_2$ (99.999%). Once 1057 °C is reached, the H$_2$ flow is reduced to 25 sccm and diluted CH$_4$ (GTS-WELCO, 1.05%, balanced by Ar) is introduced at 2 sccm. The CH$_4$ gas flow was stopped after 100 min of graphene growth and the furnace was rapidly cooled to room temperature in a flow of 1000 sccm of Ar and 7 sccm of H$_2$.

Device Preparation. Samples were based on Si wafers coated on both sides with polished 100 nm super low stress LPCVD silicon nitride (<100 MPa stress) obtained from WRS Materials. Freestanding Si$_3$N$_4$ membranes of dimensions 40 × 40 μm^2 were micromachined using standard silicon wet etching in KOH (Fisher Scientific, P251−3). Conventional lithography (Nanonex NX-2600 with Futurex NR71−1000P and JEOL 6400 with Micro-Chem 950PMMA C4) was used to pattern Au source-drain electrodes extending onto the membrane, and a 0.2−1 μm wide slit between the contacts was defined using focused ion beam milling (FEI Strata DB235). Large-area APCVD graphene was transferred onto the Si/Si$_3$N$_4$ chip and patterned into a freestanding ribbon geometry using electron beam lithography (JEOL 6400 with Dow Corning XR-1541−002) and O$_2$ plasma etching (Technics PE II-A, 30 s at 40 W). Devices consisted of an isolated graphene ribbon, ∼1 μm wide, suspended over the slit defined in the SiN$_x$ membrane and contacted by Au source-drain electrodes (a schematic of the fabrication process flow is provided in Supporting Information Figure S1).

Sample Characterization. Transmission electron microscopy was carried out on an FEI Titan 80−300 field-emission TEM with an objective-lens aberration corrector, operated at 300 kV in TEM mode. A Protochip Aduro Electrical Biasing holder was used for *in situ* electrical biasing. A National Instruments 6221 DAQ card is used to source the bias voltage and a preamplifier is used to measure the current. A custom Labview program is used to set/sweep the bias voltages in addition to record electrical measurements.

Conflict of Interest: The authors declare no competing financial interest.

Supporting Information Available: Device fabrication process flow schematic. Calculation of sputtering rate for C atoms due to the electron beam. Calculation of GNR thermal dissipation. TEM micrographs of GNR edge before and after annealing. TEM images of bonded bilayers and analysis of their twist angles. Reproduction of TEM images shown in Figure 2 from main text with dotted lines indicating the areas used to generate the 2D FFTs. This material is available free of charge *via* the Internet at http://pubs.acs.org.

REFERENCES AND NOTES

1. Gordon, M. Progress in Digital Integrated Electronics. *Tech. Dig. - Int. Electron Devices Meet.* **1975**, 11−13.
2. Moore, G. E. No Exponential is Forever: But "Forever" can be Delayed! *Dig. Tech. Pap.* **2003**, 19−25.
3. Schwierz, F. Graphene Transistors. *Nat. Nanotechnol.* **2010**, *5*, 487−496.
4. Chen, J. H.; Jang, C.; Xiao, S. D.; Ishigami, M.; Fuhrer, M. S. Intrinsic and Extrinsic Performance Limits of Graphene Devices on SiO$_2$. *Nat. Nanotechnol.* **2008**, *3*, 206−209.
5. Bolotin, K. I.; Sikes, K. J.; Jiang, Z.; Klima, M.; Fudenberg, G.; Hone, J.; Kim, P.; Stormer, H. L. Ultrahigh Electron Mobility in Suspended Graphene. *Solid State Commun.* **2008**, *146*, 351−355.

6. Balandin, A. A.; Ghosh, S.; Bao, W. Z.; Calizo, I.; Teweldebrhan, D.; Miao, F.; Lau, C. N. Superior Thermal Conductivity of Single-Layer Graphene. *Nano Lett.* **2008**, *8*, 902–907.

7. Balandin, A. A. Thermal Properties of Graphene and Nanostructured Carbon Materials. *Nat. Mater.* **2011**, *10*, 569–581.

8. Bolotin, K. I.; Sikes, K. J.; Hone, J.; Stormer, H. L.; Kim, P. Temperature-Dependent Transport in Suspended Graphene. *Phys. Rev. Lett.* **2008**, *101*, 096802.

9. Qi, Z. J.; Hong, S. J.; Rodríguez-Manzo, J. A.; Kybert, N. J.; Gudibande, R.; Drndić, M.; Park, Y. W.; Johnson, A. T. C. Electronic Transport in Heterostructures of Chemical Vapor Deposited Graphene and Hexagonal Boron Nitride. *Small* **2014**, 10.1002/smll.201402543.

10. Chen, X. Y.; Akinwande, D.; Lee, K. J.; Close, G. F.; Yasuda, S.; Paul, B. C.; Fujita, S.; Kong, J.; Wong, H. S. P. Fully Integrated Graphene and Carbon Nanotube Interconnects for Gigahertz High-Speed CMOS Electronics. *IEEE Trans. Electron Devices* **2010**, *57*, 3137–3143.

11. Behnam, A.; Lyons, A. S.; Bae, M. H.; Chow, E. K.; Islam, S.; Neumann, C. M.; Pop, E. Transport in Nanoribbon Interconnects Obtained from Graphene Grown by Chemical Vapor Deposition. *Nano Lett.* **2012**, *12*, 4424–4430.

12. Schwierz, F. Graphene Transistors: Status, Prospects, and Problems. *Proc. IEEE* **2013**, *101*, 1567–1584.

13. Lin, Y. M.; Valdes-Garcia, A.; Han, S. J.; Farmer, D. B.; Meric, I.; Sun, Y. N.; Wu, Y. Q.; Dimitrakopoulos, C.; Grill, A.; Avouris, P.; *et al.* Wafer-Scale Graphene Integrated Circuit. *Science* **2011**, *332*, 1294–1297.

14. Hill, E. W.; Vijayaragahvan, A.; Novoselov, K. Graphene Sensors. *IEEE Sens. J.* **2011**, *11*, 3161–3170.

15. Lu, Y.; Lerner, M. B.; Qi, Z. J.; Mitala, J. J.; Lim, J. H.; Discher, B. M.; Johnson, A. T. C. Graphene-Protein Bioelectronic Devices with Wavelength-Dependent Photoresponse. *Appl. Phys. Lett.* **2012**, *100*, 033110.

16. Kybert, N. J.; Han, G. H.; Lerner, M. B.; Dattoli, E. N.; Esfandiar, A.; Johnson, A. T. C. Scalable Arrays of Chemical Vapor Sensors Based on DNA-Decorated Graphene. *Nano Res.* **2014**, *7*, 95–103.

17. Pan, M.; Girão, E. C.; Jia, X.; Bhaviripudi, S.; Li, Q.; Kong, J.; Meunier, V.; Dresselhaus, M. S. Topographic and Spectroscopic Characteriztion of Electronic Edge States in CVD Grown Graphene Nanoribbons. *Nano Lett.* **2012**, *12*, 1928–1933.

18. Cai, J.; Ruffieux, P.; Jaafar, R.; Bieri, M.; Braun, T.; Blankenburg, S.; Muoth, M.; Seitsonen, A. P.; Saleh, M.; Feng, X.; *et al.* Atomically Precise Bottom-Up Fabricatino of Graphene Nanoribbons. *Nature* **2010**, *466*, 470–473.

19. Cai, J.; Pignedoli, C. A.; Talirz, L.; Ruffieux, P.; Sode, H.; Liang, L.; Meunier, V.; Berger, R.; Li, R.; Feng, X.; *et al.* Graphene Nanoribbon Heterojunctions. *Nat. Nanotechnol.* **2014**, *9*, 896–900.

20. Han, M. Y.; Ozyilmaz, B.; Zhang, Y. B.; Kim, P. Energy Band-Gap Engineering of Graphene Nanoribbons. *Phys. Rev. Lett.* **2007**, *98*, 206805.

21. Bai, J. W.; Duan, X. F.; Huang, Y. Rational Fabrication of Graphene Nanoribbons Using a Nanowire Etch Mask. *Nano Lett.* **2009**, *9*, 2083–2087.

22. Lu, Y.; Goldsmith, B.; Strachan, D. R.; Lim, J. H.; Luo, Z. T.; Johnson, A. T. C. High-On/Off-Ratio Graphene Nanoconstriction Field-Effect Transistor. *Small* **2010**, *6*, 2748–2754.

23. Tapaszto, L.; Dobrik, G.; Lambin, P.; Biro, L. P. Tailoring the Atomic Structure of Graphene Nanoribbons by Scanning Tunnelling Microscope Lithography. *Nat. Nanotechnol.* **2008**, *3*, 397–401.

24. Bai, J. W.; Zhong, X.; Jiang, S.; Huang, Y.; Duan, X. F. Graphene Nanomesh. *Nat. Nanotechnol.* **2010**, *5*, 190–194.

25. Areshkin, D. A.; Gunlycke, D.; White, C. T. Ballistic Transport in Graphene Nanostrips in the Presence of Disorder: Importance of Edge Effects. *Nano Lett.* **2007**, *7*, 204–210.

26. Basu, D.; Gilbert, M. J.; Register, L. F.; Banerjee, S. K.; MacDonald, A. H. Effect of Edge Roughness on Electronic Transport in Graphene Nanoribbon Channel Metal-Oxide-Semiconductor Field-Effect Transistors. *Appl. Phys. Lett.* **2008**, *92*, 042114.

27. Goharrizi, A. Y.; Pourfath, M.; Fathipour, M.; Kosina, H. Device Performance of Graphene Nanoribbon Field-Effect Transistors in the Presence of Line-Edge Roughness. *IEEE Trans. Electron Devices* **2012**, *59*, 3527–3532.

28. Fischbein, M. D.; Drndic, M. Electron Beam Nanosculpting of Suspended Graphene Sheets. *Appl. Phys. Lett.* **2008**, *93*, 113107.

29. Borrnert, F.; Fu, L.; Gorantla, S.; Knupfer, M.; Buchner, B.; Rummeli, M. H. Programmable Sub-nanometer Sculpting of Graphene with Electron Beams. *ACS Nano* **2012**, *6*, 10327–10334.

30. Song, B.; Schneider, G. F.; Xu, Q.; Pandraud, G.; Dekker, C.; Zandbergen, H. Atomic-Scale Electron-Beam Sculpting of Near-Defect-Free Graphene Nanostructures. *Nano Lett.* **2011**, *11*, 2247–2250.

31. Qi, Z. J.; Rodríguez-Manzo, J. A.; Hong, S. J.; Park, Y. W.; Stach, E. A.; Drndić, M.; Johnson, A. T. C. Direct Electron Beam Patterning of Sub-5nm Monolayer Graphene Interconnects. *Proc. SPIE* **2013**, *8680*, 86802F–86802F-6.

32. Meyer, J. C.; Eder, F.; Kurasch, S.; Skakalova, V.; Kotakoski, J.; Park, H. J.; Roth, S.; Chuvilin, A.; Eyhusen, S.; Benner, G.; *et al.* Accurate Measurement of Electron Beam Induced Displacement Cross Sections for Single-Layer Graphene. *Phys. Rev. Lett.* **2012**, *108*, 196102.

33. Xu, Q.; Wu, M. Y.; Schneider, G. F.; Houben, L.; Malladi, S. K.; Dekker, C.; Yucelen, E.; Dunin-Borkowski, R. E.; Zandbergen, H. W. Controllable Atomic Scale Patterning of Freestanding Monolayer Graphene at Elevated Temperature. *ACS Nano* **2013**, *7*, 1566–1572.

34. Lu, Y.; Merchant, C. A.; Drndic, M.; Johnson, A. T. C. *In Situ* Electronic Characterization of Graphene Nanoconstrictions Fabricated in a Transmission Electron Microscope. *Nano Lett.* **2011**, *11*, 5184–5188.

35. Qi, Z. J.; Rodríguez-Manzo, J. A.; Botello-Méndez, A. R.; Hong, S. J.; Stach, E. A.; Park, Y. W.; Charlier, J.-C.; Drndić, M.; Johnson, A. T. C. Correlating Atomic Structure and Transport in Suspended Graphene Nanoribbons. *Nano Lett.* **2014**, *14*, 4238–4244.

36. Jia, X. T.; Hofmann, M.; Meunier, V.; Sumpter, B. G.; Campos-Delgado, J.; Romo-Herrera, J. M.; Son, H. B.; Hsieh, Y. P.; Reina, A.; Kong, J.; *et al.* Controlled Formation of Sharp Zigzag and Armchair Edges in Graphitic Nanoribbons. *Science* **2009**, *323*, 1701–1705.

37. Westenfelder, B.; Meyer, J. C.; Biskupek, J.; Kurasch, S.; Scholz, F.; Krill, C. E.; Kaiser, U. Transformations of Carbon Adsorbates on Graphene Substrates under Extreme Heat. *Nano Lett.* **2011**, *11*, 5123–5127.

38. Chen, J.; Shi, T.; Cai, T.; Xu, T.; Sun, L.; Wu, X.; Yu, D. Self Healing of Defected Graphene. *Appl. Phys. Lett.* **2013**, *102*, 103107.

39. Zan, R.; Ramasse, Q. M.; Bangert, U.; Novoselov, K. S. Graphene Reknits Its Holes. *Nano Lett.* **2012**, *12*, 3936–3940.

40. Börrnert, F.; Barreiro, A.; Wolf, D.; Katsnelson, M. I.; Büchner, B.; Vandersypen, L. M. K.; Rümmeli, M. H. Lattice Expansion in Seamless Bilayer Graphene Constrictions at High Bias. *Nano Lett.* **2012**, *12*, 4455–4459.

41. Barreiro, A.; Borrnert, F.; Rummeli, M. H.; Buchner, B.; Vandersypen, L. M. K. Graphene at High Bias: Cracking, Layer by Layer Sublimation, and Fusing. *Nano Lett.* **2012**, *12*, 1873–1878.

42. Rümmeli, M. H.; Rocha, C. G.; Ortmann, F.; Ibrahim, I.; Sevincli, H.; Börrnert, F.; Kunstmann, J.; Bachmatiuk, A.; Pötschke, M.; Shiraishi, M.; *et al.* Graphene: Piecing it Together. *Adv. Mater.* **2011**, *23*, 4471–4490.

43. Schmidt, H.; Rode, J. C.; Smirnov, D.; Haug, R. J. Superlattice Structures in Twisted Bilayers of Folded Graphene. *Nat. Commun.* **2014**, *5*, 5742.

44. Luo, Z.; Lu, Y.; Singer, D. W.; Berck, M. E.; Somers, L. A.; Goldsmith, B. R.; Johnson, A. T. C. Effect of Substrate Roughness and Feedstock Concentration on Growth of Wafer-Scale Graphene at Atmospheric Pressure. *Chem. Mater.* **2011**, *23*, 1441–1447.

45. Luo, Z.; Kim, S.; Kawamoto, N.; Rappe, A. M.; Johnson, A. T. C. Growth Mechanism of Hexagonal-Shape Graphene Flakes with Zigzag Edges. *ACS Nano* **2011**, *5*, 9154–9160.

46. Qi, Z. J.; Johnson, A. T. C. Facile Fabrication of Nanogap Electrodes for Suspended Graphene Characterization Using Direct Ion Beam Patterning. *Proc. SPIE* **2014**, *8973*, 89730P–89730P-6.

47. Moser, J.; Barreiro, A.; Bachtold, A. Current-Induced Cleaning of Graphene. *Appl. Phys. Lett.* **2007**, *91*, 163513.

48. Meyer, J. C.; Girit, C. O.; Crommie, M. F.; Zettl, A. Hydrocarbon Lithography on Graphene Membranes. *Appl. Phys. Lett.* **2008**, *92*, 123110.

49. Liu, Z.; Suenaga, K.; Harris, P. J. F.; Iijima, S. Open and Closed Edges of Graphene Layers. *Phys. Rev. Lett.* **2009**, *102*, 015501.

50. Huang, J. Y.; Ding, F.; Yakobson, B. I.; Lu, P.; Qi, L.; Li, J. *In Situ* Observation of Graphene Sublimation and Multi-Layer Edge Reconstructions. *Proc. Natl. Acad. Sci. U. S. A.* **2009**, *106*, 10103–10108.

51. Cruz-Silva, E.; Jia, X.; Terrones, H.; Sumpter, B. G.; Terrones, M.; Dresselhaus, M. S.; Meunier, V. Edge-Edge Interactions in Stacked Graphene Nanoplatelets. *ACS Nano* **2013**, *7*, 2834–2841.

52. Zhang, C.; Bets, K.; Lee, S. S.; Sun, Z.; Mirri, F.; Colvin, V. L.; Yakobson, B. I.; Tour, J. M.; Hauge, R. H. Closed-Edged Graphene Nanoribbons from Large-Diameter Collapsed Nanotubes. *ACS Nano* **2012**, *6*, 6023–6032.

53. Haskins, J.; Kinaci, A.; Sevik, C.; Sevincli, H.; Cuniberti, G.; Cagin, T. Control of Thermal and Electronic Transport in Defect-Engineered Graphene Nanoribbons. *ACS Nano* **2011**, *5*, 3779–87.

54. Mucciolo, E. R.; Castro Neto, A. H.; Lewenkopf, C. H. Conductance Quantization and Transport Gaps in Disordered Graphene Nanoribbons. *Phys. Rev. B: Condens. Matter Mater. Phys.* **2009**, *79*, 075407.

55. Liang, L.; Cruz-Silva, E.; Girão, E.; Meunier, V. Enhanced Thermoelectric Figure of Merit in Assembled Graphene Nanoribbons. *Phys. Rev. B: Condens. Matter Mater. Phys.* **2012**, *86*, 115438.

56. Warner, J. H.; Rummeli, M. H.; Ge, L.; Gemming, T.; Montanari, B.; Harrison, N. M.; Buchner, B.; Briggs, G. A. D. Structural Transformations in Graphene Studied with High Spatial and Temporal Resolution. *Nat. Nanotechnol.* **2009**, *4*, 500–504.

57. Engelund, M.; Fürst, J. A.; Jauho, A. P.; B, M. Localized Edge Vibrations and Edge Reconstruction by Joule Heating. *Phys. Rev. Lett.* **2010**, *104*, 036807.

58. Bullard, Z.; Meunier, V. Dynamical Properties of Carbon Nanotube Welding into X Junctions. *Phys. Rev. B: Condens. Matter Mater. Phys.* **2013**, *88*, 035422.

59. Daniels, C.; Bullard, Z.; Girão, E. C.; Meunier, V. Emergent Magnetism in Irradiated Graphene Nanostructures. *Carbon* **2014**, *78*, 196–203.

60. Stuart, S. J.; Tutein, A. B.; Harrison, J. A. A Reactive Potential for Hydrocarbons with Intermolecular Interactions. *J. Chem. Phys.* **2000**, *112*, 6472–6486.

61. Brenner, D. W.; Shenderova, O. A.; Harrison, J. A.; Stuart, S. J.; Ni, B.; Sinnott, S. B. A Second-Generation Reactive Empirical Bond Order (REBO) Potential Energy Expression for Hydrocarbons. *J. Phys.: Condens. Matter* **2002**, *14*, 783.

62. Yazyev, O. V. Emergence of Magnetism in Graphene Materials and Nanostructures. *Rep. Prog. Phys.* **2010**, *73*, 056501.

63. Gunlycke, D.; White, C. T. Tight-Binding Energy Dispersions of Armchair-Edge Graphene Nanostrips. *Phys. Rev. B: Condens. Matter Mater. Phys.* **2008**, *77*, 115116.

64. Landauer, R. Electrical Resistance of Disordered One-Dimensional Lattices. *Philos. Mag.* **1970**, *21*, 863.

65. Nardelli, M. B. Electronic Transport in Extended Systems: Application to Carbon Nanotubes. *Phys. Rev. B: Condens. Matter Mater. Phys.* **1999**, *60*, 7828–7833.

66. Sancho, M. P. L.; Sancho, J. M. L.; Rubio, J. Quick Iterative Scheme for the Calculation of Transfer-Matrices—Application to Mo(100). *J. Phys. F: Met. Phys.* **1984**, *14*, 1205–1215.

67. Kazymyrenko, K.; Waintal, X. Knitting Algorithm for Calculating Green Functions in Quantum Systems. *Phys. Rev. B: Condens. Matter Mater. Phys.* **2008**, *77*, 115119.

68. Costa Girão, E.; Meunier, V. Patchwork Algorithm for the Parallel Computation of the Green's Function in Open Systems. *J. Comput. Electron.* **2013**, *12*, 123–133.

69. Costa Girão, E.; Cruz-Silva, E.; Meunier, V. Electronic Transport Properties of Assembled Carbon Nanoribbons. *ACS Nano* **2012**, *6*, 6483–6491.

70. Botello-Mendez, A. R.; Cruz-Silva, E.; Romo-Herrera, J. M.; Lopez-Urias, F.; Terrones, M.; Sumpter, B. G.; Terrones, H.; Charlier, J. C.; Meunier, V. Quantum Transport in Graphene Nanonetworks. *Nano Lett.* **2011**, *11*, 3058–3064.